

Creep Performance and Microstructural Characterization of Electron-Beam Welded 316LN SS-Grade 91 Steel Dissimilar Joint



J. VANAJA, H.C. DEY, G.V. PRASAD REDDY, K. LAHA, and M. VASUDEVAN

Microstructural features and creep-rupture behaviour of a dissimilar weld joint (DWJ) between Grade 91 (G91) steel and 316LN stainless steel prepared by Electron beam (EB) welding are investigated. The SEM-EDAX and EBSD observations in the fusion zone revealed compositional variations and distinct microstructural features, depending on the extent of mixing of both base metals. Further, at the interface between the fusion zone and G91 steel, nickel enrichment was observed, which lowered the A_{c1} temperature, resulting in fresh martensite and higher hardness upon PWHT. In the creep-rupture tests conducted at 873 K and 110 to 175 MPa, failure location shifted from G91 base metal to intercritical HAZ of G91 steel above 2500 hours of creep exposure. As against the interface failures, which are considered the life-limiting factor in DWJs, the ruptured specimens in the present study revealed better interface stability with insignificant cavitation even after creep exposure of over 10,000 hours. The composition at the ferritic–weld interface exhibits almost equivalent carbon activity to G91 steel which improved the interface stability by resisting the coarsening of carbides. It is important to highlight that the EB weld joint exhibited higher rupture life and weld strength reduction factor than the joints made by conventional multi-pass arc welding.

<https://doi.org/10.1007/s11661-023-07074-0>

© The Minerals, Metals & Materials Society and ASM International 2023

I. INTRODUCTION

IN power plants, austenitic stainless steel (SS) is generally used in high-temperature sections, where creep rupture strength and oxidation resistance are crucial. In contrast, Cr–Mo ferritic–martensitic steels are used at comparatively lower temperatures. From an economic and operational perspective, dissimilar weld joints (DWJs) between Cr–Mo ferritic–martensitic steels and austenitic stainless steels are recommended. In such joints, chemical composition, microstructure, stress state, physical properties and mechanical properties are appreciably different across the weldment and are generally considered the weakest link in the entire mechanical structure.

Evans and Wilshire have reported that in the early UK boiler designs, DWJs fabricated by the Flash Butt Welding Process, which forms a direct ferritic–austenitic bond, had shown poor service experience and were abandoned and replaced with GTAW/MMAW processes.^[1] Later, there has been evolution in design for welding consumables. In the past, austenitic steel filler wire was used for such DWJs. Lundin reviewed failures of transition joints and reported that the joints failed prematurely before the expected lifetime of the structure under elevated temperature conditions in operation.^[2] The failures were attributed to the presence of the wider untempered martensitic region at the interface between fusion zone and ferritic base metal (mentioned hereafter as “ferritic–weld interface”) and the carbon migration issues leading to the formation of carbon denuded zone, coarse carbides, sigma phase *etc.*, in and around the ferritic–weld interface. In practice, nickel-based welding consumables are recommended for such joints using conventional welding techniques to reduce the carbon migration issues.^[3] Ni-based welding consumables reduces the carbon activity gradient between ferritic steel and austenitic stainless steel. It has also been reported that the repulsive interaction of carbon atoms with Ni limits the carbon migration issues near the ferritic–weld interface.^[4–6] However, in DWJs produced using nickel-based consumables, long-term creep failure is observed prematurely at the interface between ferritic

J. VANAJA and G.V. PRASAD REDDY, and M. VASUDEVAN are with the Metallurgy and Materials Group, Indira Gandhi Centre for Atomic Research, Kalpakkam 603102, India and also with the Homi Bhabha National Institute, Training School Complex, Anushaktinagar, Mumbai 400094, India. Contact e-mail: jvanaja@igcar.gov.in H.C. DEY and K. LAHA are with the Metallurgy and Materials Group, Indira Gandhi Centre for Atomic Research.

Manuscript submitted August 27, 2022; accepted April 20, 2023.

Article published online May 18, 2023

steel and weld metal.^[7–9] Some of the possible reasons reported for premature failure of the DWJs as reviewed by Dupont are cyclic thermal stresses, low oxidation resistance of ferritic steel leading to oxide notch at its interface, carbon migration from ferritic steel to the weld interface leading to a series of carbide formation along with the interface, and metallurgical degradation (e.g. the formation of coarse carbides, sigma phase) caused by high-temperature conditions in service.^[10]

A schematic illustration of the failure location of the ferritic–austenitic DWJ specimens during creep exposure is represented in Figure 1 as a function of stress and creep rupture life.^[7–9] It may be noted that, for the illustration in Figure 1, the base metals considered include ferritic steels like 2.25Cr–1Mo steel, plain 9Cr–1Mo and modified 9Cr–1Mo (Grade 91) steel and austenitic materials like Alloy 800 and 316 SS welded with Ni-based welding consumables. At higher stress levels, cup and cone type ductile dimple fracture is observed on the ferritic–martensitic base metal and is not encountered during actual service. The failure location shifts to the intercritical HAZ with a decrease in stress and is predominantly intergranular creep failure termed as type IV failure. This is associated with a change in the slope of the stress-rupture plot. The exposure time for Type IV failure is dependent on the testing temperature, and it is short at higher test temperatures. At further lower stresses (long-term creep exposure of practical relevance to a power plant), the failure location is shifted to the ferritic–weld interface. The failure is associated with the nucleation, growth, and coalescence of creep cavities at particles along the ferritic–weld interface. This kind of failure is accompanied by a steeper slope change in stress-rupture plot and being catastrophic research efforts are in progress to delay/circumvent such failures.

Research efforts have been in progress worldwide to circumvent the interface failures in DWJs between ferritic and austenitic alloys by altering the filler wire's composition or developing novel fabrication techniques. One such study involves the development of nickel-base filler metal to match the coefficient of thermal expansion with ferritic steel and reduce carbon migration across the fusion line. Commercially, the filler metal is named

P87, and the studies have shown improvement in the creep strength of weld joints prepared using P87 filler wire.^[11] Another development that emerged in the fabrication methodology pertains to functionally graded transition joints (GTJs). Such joints are made by additively depositing layers of alloy A with increasing dilution levels (0 to 100 pct) on an alloy B substrate or vice versa. This design concept has been adopted in ferritic–austenitic dissimilar joints. It is also reported that such joints possess gradual transitions in chemical composition, microstructure, and mechanical properties from one base metal to the other base metal.^[12–14] Such joints have been successful in circumventing the problem of interfacial failure. The technology is being developed for industrial applications.

Autogenous welding of the dissimilar joint was never recommended in power plant component fabrication as it results in highly inhomogeneous weld chemistry. Hence, the weld joints are fabricated commercially by gas tungsten arc welding (GTAW) or manual metal arc welding (MMAW) techniques using appropriate consumables. However, in such techniques, multiple passes are deposited for welding thick sections, wherein each pass induces a thermal cycle in the base metals. Laha *et al.* have shown that materials like Grade 91 steel (G91), when subjected to weld thermal cycle, undergo phase changes leading to the complex microstructural changes in the heat-affected zone (HAZ).^[15] The recent development of novel welding technologies with high power density and low heat input, such as electron beam and laser welding, produces narrow fusion zone and HAZ compared to conventional welding techniques like GTAW or MMAW. A very recommended using techniques such as electron beam, laser, and pulsed arc to weld dissimilar metals under the category of low dilution welds since the amount of base metal melted is relatively small and filler metals are not generally used.^[16] Sun *et al.* have reviewed the EB welding of dissimilar metals, with special emphasis on demonstrating the potential of the process for producing high-quality DWJs.^[17] Thus, the apprehension of inhomogeneous weld chemistry over a large region and cumulative damage to the base metal due to weld thermal cycle can be extensively reduced using novel welding techniques. An understanding of the microstructural changes across the weldment and its performance under creep conditions is of primary concern in the design of welded structures. The current investigation presents microstructural features and creep-rupture behaviour of a bimetallic DWJ between G91 steel and 316LN SS prepared by electron-beam welding.

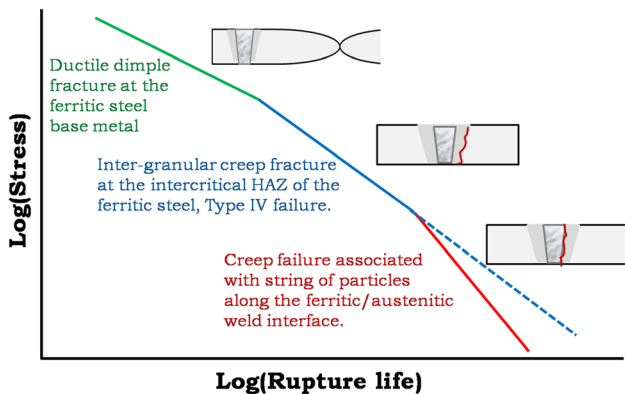


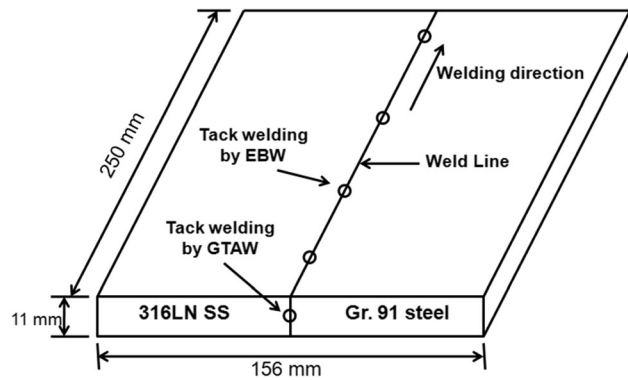
Fig. 1—Failure locations in ferritic–austenitic dissimilar weld joint as a function of stress and rupture life.

II. EXPERIMENTAL DETAILS

The chemical composition of the G91 steel and 316LN SS plates used is shown in Table I. The 316LN SS was used in the solution annealed condition (1373 K for 1 hour and water-quenched), and G91 steel was used in Normalized (1323 K for 15 minutes and air-cooled) and tempered (1053 K for 1 hour and air-cooled) condition. A dissimilar weld joint of G91 steel and

Table I. Chemical Composition of Base Metals 316LN SS and G91 Steel Used in the Study in Wt. Pct

	C	Cr	Ni	Mn	Si	P	S	N	Mo	Nb	V	Fe
316LN	0.027	17.53	12.2	1.7	0.22	0.013	0.005	0.07	2.49	—	—	bal
G91	0.11	8.84	0.22	0.403	0.309	0.014	0.0008	0.0538	0.86	0.08	0.207	bal

**Fig. 2—Schematic of electron beam welded dissimilar joint configuration.****Table II. Welding Parameters Used for Weld Pad Fabrication Using EBW Process**

Welding Parameters	Full Penetration Weld	Cosmetic Pass
Beam Current	128 mA	40 mA
Gun Voltage	60 kV	60 kV
Welding Speed	800 mm/min	800 mm/min

316LN SS was fabricated by the electron-beam welding (EBW) technique using 11 mm thick plates. Figure 2 shows the schematic of square-butt joint configuration, fit-up and plate dimensions used for fabrication of weld joint. The 11 mm thick G91 steel and 316LN SS plates were welded by autogenous (without filler wire addition) EBW process in a single pass. To smoothen the weld face and better weld bead appearance, a cosmetic pass with lower heat input was performed. Details of the welding parameters are furnished in Table II. The weld pad was qualified for its soundness using X-ray radiography. The radiography inspection revealed no welding defects. Subsequently, the weld joint was subjected to post-weld heat treatment (PWHT) at 1033 K for three hours. Cross weld creep specimens were extracted from the weld joint in such a way that each of the specimens contained a weld (fusion) zone at the centre of the gauge length. Uniaxial creep tests were carried out at 873 K over the stress range of 175 to 110 MPa. The test temperature was maintained within ± 2 K during the creep test.

A detailed microstructural investigation was carried out using optical and scanning electron microscopy. For revealing the microstructure of the 316LN SS and fusion zone, electrolytic etching (at room temperature, ~ 1.0 V

DC for 5 to 10 seconds) was carried out using 60 pct nitric acid in the water, and for the ferritic steel, swab etching was done using Vilella's reagent. Microchemical investigations across the joint were carried out using SEM-EDAX. Spot analysis was carried out across the weld joint and near creep failure location to quantify the major alloying elements and to predict the phases present in the microstructure. Electron backscattered diffraction (EBSD) scanning across the ferritic–weld interface region was performed with a $0.075 \mu\text{m}$ step size. EBSD data were analysed using HKL[®] channel-5 software, and Phase map, Band slope map and Kernel average misorientation (KAM) map with misorientations 0.1 to 3 deg were obtained. JMatPro[®] simulation software was used to determine the transformation temperature of the G91 steel and also for the chemical composition obtained from spot analysis at the ferritic–weld interface. It uses a CALPHAD-based internal database for the calculation, and the 'General steel' module available in "JMatPro[®] version 7" was used in this study. The calculation for carbon activity of base metals was performed using Calphad-based Thermo-Calc[™] software version S with TCFE8 database for steels. Microhardness profiles across the joint were obtained using a Vickers hardness tester employing a load of 50 gf, and the standard deviation in hardness is ± 5 Hv in the as-welded and PWHT conditions.

III. RESULTS

A. Microstructure

The macrostructure of the weld joint comprising of base metals and fusion zone is shown in Figure 3(a). The figure shows a 'wine glass' shaped weld (fusion zone) sandwiched between the two base metals. The microstructure across the joint consisted of austenitic structure on the 316LN SS side, tempered martensitic structure on the G91 steel side and inhomogeneously mixed weld structure in the fusion zone. Figure 3(b) shows the interface structure of the fusion zone with 316LN SS base metal. No significant microstructural changes were observed in 316LN SS HAZ. However, epitaxial growth of dendrites in the weld originating from the partially melted grains of the 316LN SS base metal, as indicated in Figure 3(b), is observed. Figure 3(c) shows the presence of various solidification substructures in the fusion zone. It comprised both cellular and columnar dendritic structures. Figure 3(d) shows the weld interface between the fusion zone and the G91 steel in polarised contrast. The polarized image reveals the microstructure at the ferritic–weld interface as the microstructure in this region and on G91 HAZ

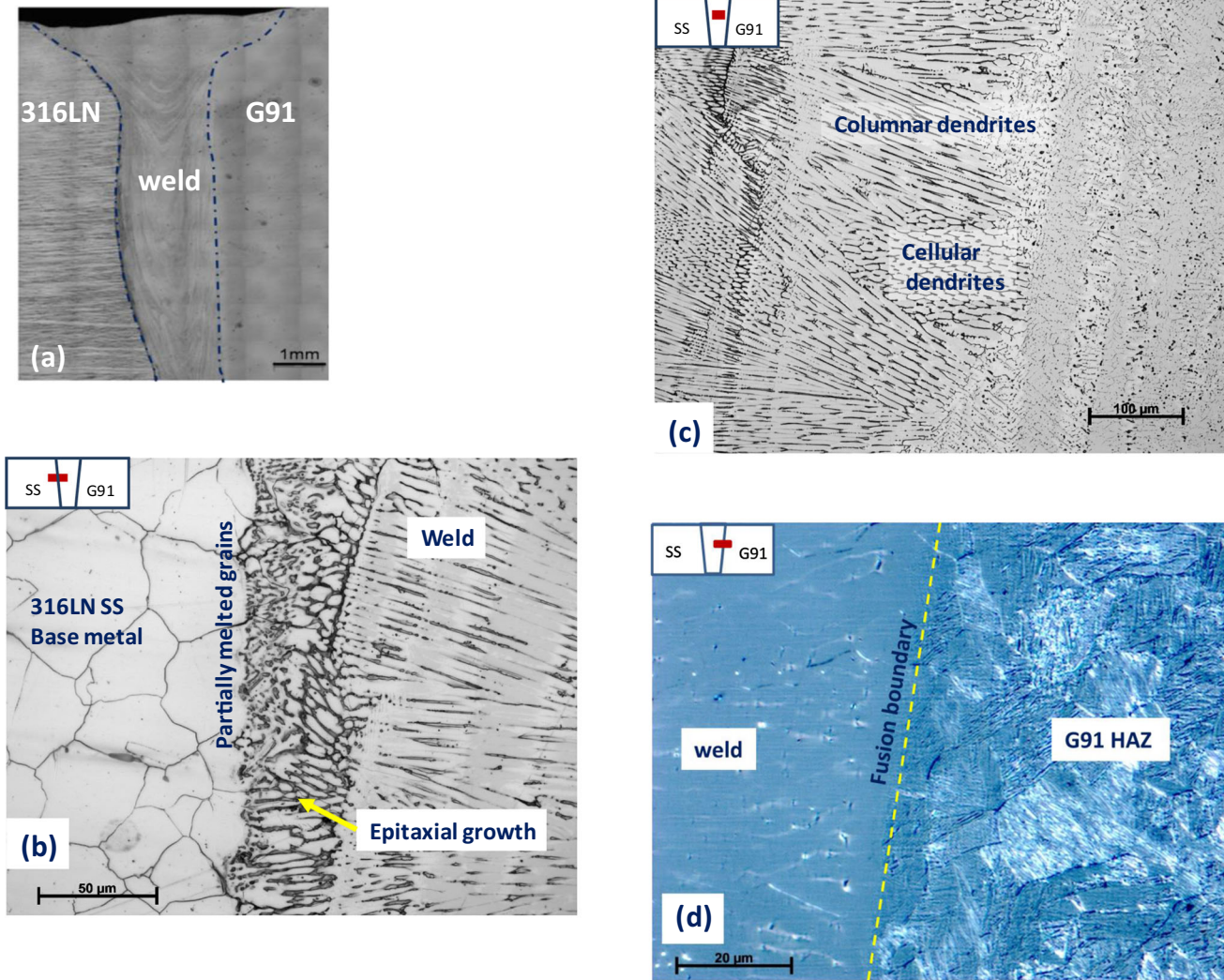


Fig. 3—Optical micrographs of dissimilar joint across the weldment: (a) Macrostructure of the weld joint; the zone within dotted lines indicates wine glass shaped weld. (b) 316LN–weld interface, (c) a region from fusion zone showing various solidification substructures and (d) weld–G91 steel interface in polarised contrast.

are not discernable in bright field contrast due to the untempered martensitic phase.

The various solidification sub-structures in the micrograph of the fusion zone assert the presence of different phases formed during welding. Identification of the phases present in the fusion zone is of utmost importance from the viewpoint of microstructural influence on resultant mechanical properties. An attempt to predict the phases present in the fusion zone using Schaeffler diagram^[18] was carried out by calculating the chromium equivalent ($\text{wt. pct Cr} + \text{wt. pct Mo} + 1.5 \times \text{wt. pct Si} + 0.5 \times \text{wt. pct Nb}$) and nickel equivalent ($\text{wt. pct Ni} + 30 \times \text{wt. pct C} + 0.5 \times \text{wt. pct Mn}$) across the fusion zone. Assuming 50 pct dilution from both the parent metals, the Cr and Ni equivalents of the fusion zone have been estimated to be 15.3 and 10.7, respectively. This composition suggests the presence of both Austenite and Martensite (A + M) in the fusion zone as per the Schaeffler diagram shown in Figure 4.

In order to analyse in detail fusion zone microstructure, EDS spot analysis was performed at a spacing of 0.25 mm across the fusion zone in the as-welded sample, as shown in the micrograph in Figure 4, to corroborate the above-mentioned prediction. The main elements measured were Cr, Ni, Mo, Nb, Mn, Si and Fe(balance). The measured compositions at each location were converted into Ni and Cr equivalents as per the previously mentioned equations and plotted onto the Schaeffler diagram (Figure 4). It is to be noted that the carbon content used for the calculation was taken from the composition of the weld metal calculated by assuming equal dilution (50 pct) of both parent metals, as mentioned earlier. The EDS compositions, taken from the fusion zone, fall in the A + M + F region (Austenite + Martensite + Ferrite).

After PWHT a significant microstructural change is observed in the ferritic HAZ. It is well known that the carbides present in G91 steel are M_{23}C_6 and MX type carbides and carbonitrides.^[15] During weld thermal

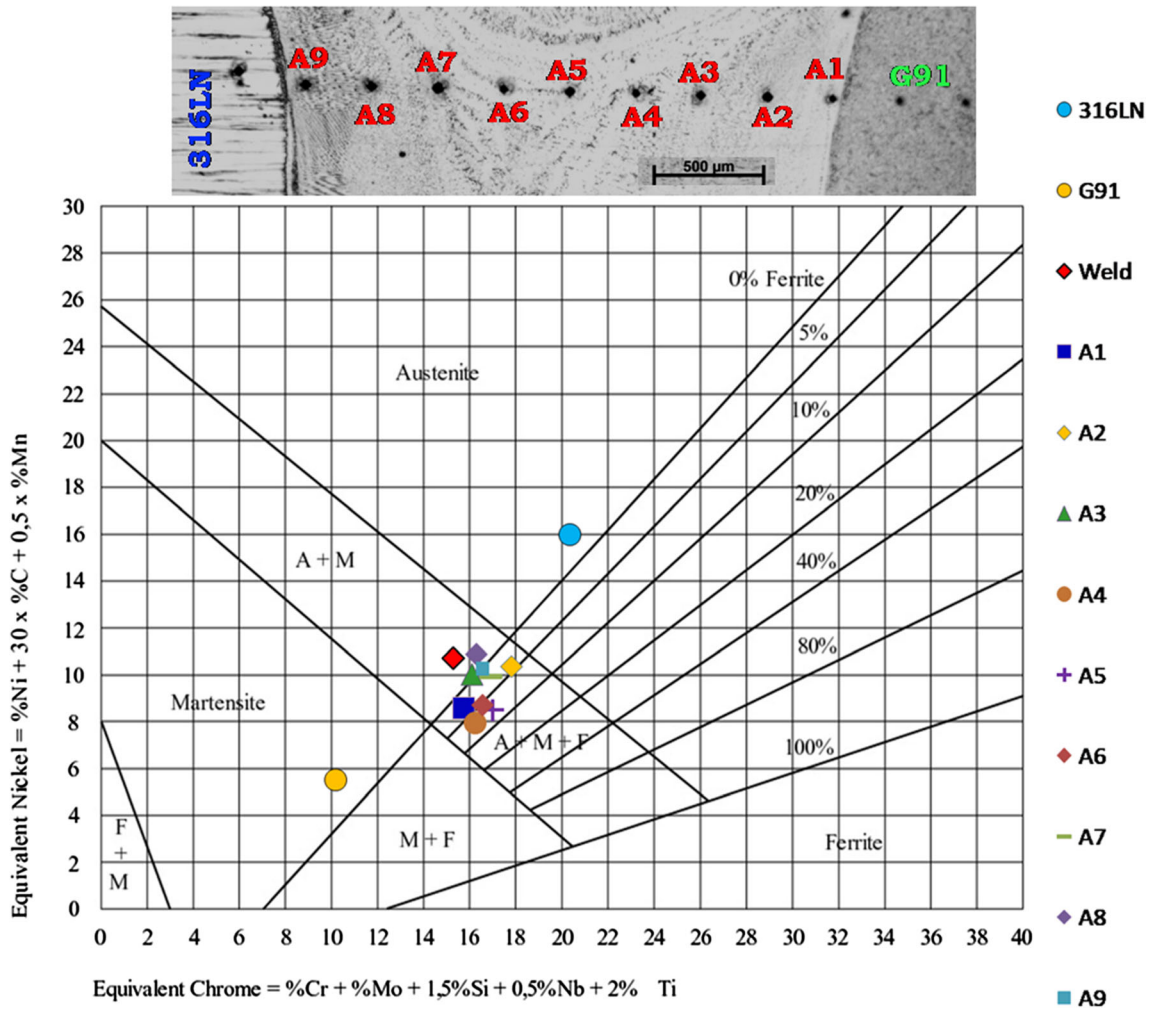


Fig. 4—Schaeffler diagram representing phases present in the dissimilar weldment.

cycle, depending on the temperature exposed by the HAZ region, the dissolution or partial dissolution of $M_{23}C_6$ precipitates occurs predominantly and hence the prior austenite grain size and distribution of $M_{23}C_6$ precipitates varies across each regime of HAZ. Figures 5(a) through (d) shows the microstructure of HAZ in G91 steel after PWHT. The width of the HAZ adjacent to the fusion boundary is around 0.7 mm. The regions within the HAZ have continuously varying microstructures depending on the peak temperature experienced during welding. The region adjacent to the ferritic-weld interface consists of coarse-grained HAZ (CGHAZ) (Figure 5(a)), which is exposed to a temperature range well above the Ac_3 transformation temperature (~ 1167 K). As a result, upon heating, the tempered martensite transforms to austenite, with nearly complete dissolution of $M_{23}C_6$ precipitates, causing significant growth of the austenite grains during welding. After PWHT, the $M_{23}C_6$ carbides precipitate on the lath/grain boundaries and are comparatively finer.

In the next adjoining region, *i.e.* fine-grained heat-affected zone (FGHAZ) (Figure 5(b)), which is subjected to a temperature range just above Ac_3 , the combination

of time and temperature is inadequate for the complete dissolution of precipitates. Thus, austenite grain growth is limited by the incomplete dissolution of carbides, nitrides or carbo-nitrides. The intercritical heat-affected zone (ICHAZ), which is next to the FGHAZ, is confined to a temperature range between the Ac_1 and Ac_3 transformation temperatures (Figure 5(c)). This region undergoes partial transformation to austenite without significant dissolution of $M_{23}C_6$ carbides. The newly formed austenite predominantly transforms to martensite on cooling, and the untransformed tempered martensite gets recovered to a greater extent following PWHT. The exposure to the intercritical temperature range and subsequent PWHT coarsens the $M_{23}C_6$ precipitates in the ICHAZ. It must be mentioned that the carbides shown in the images correspond to $M_{23}C_6$ carbides based on the EDS analysis. A typical high resolution image of $M_{23}C_6$ carbides at ICHAZ region along with its EDS characterization is shown in Figure 5(e). Figure 5(d) illustrates the microstructure of the base metal region unaffected by the weld thermal cycle where lenticular $M_{23}C_6$ precipitates arranged on the lath/grain boundaries could be observed.

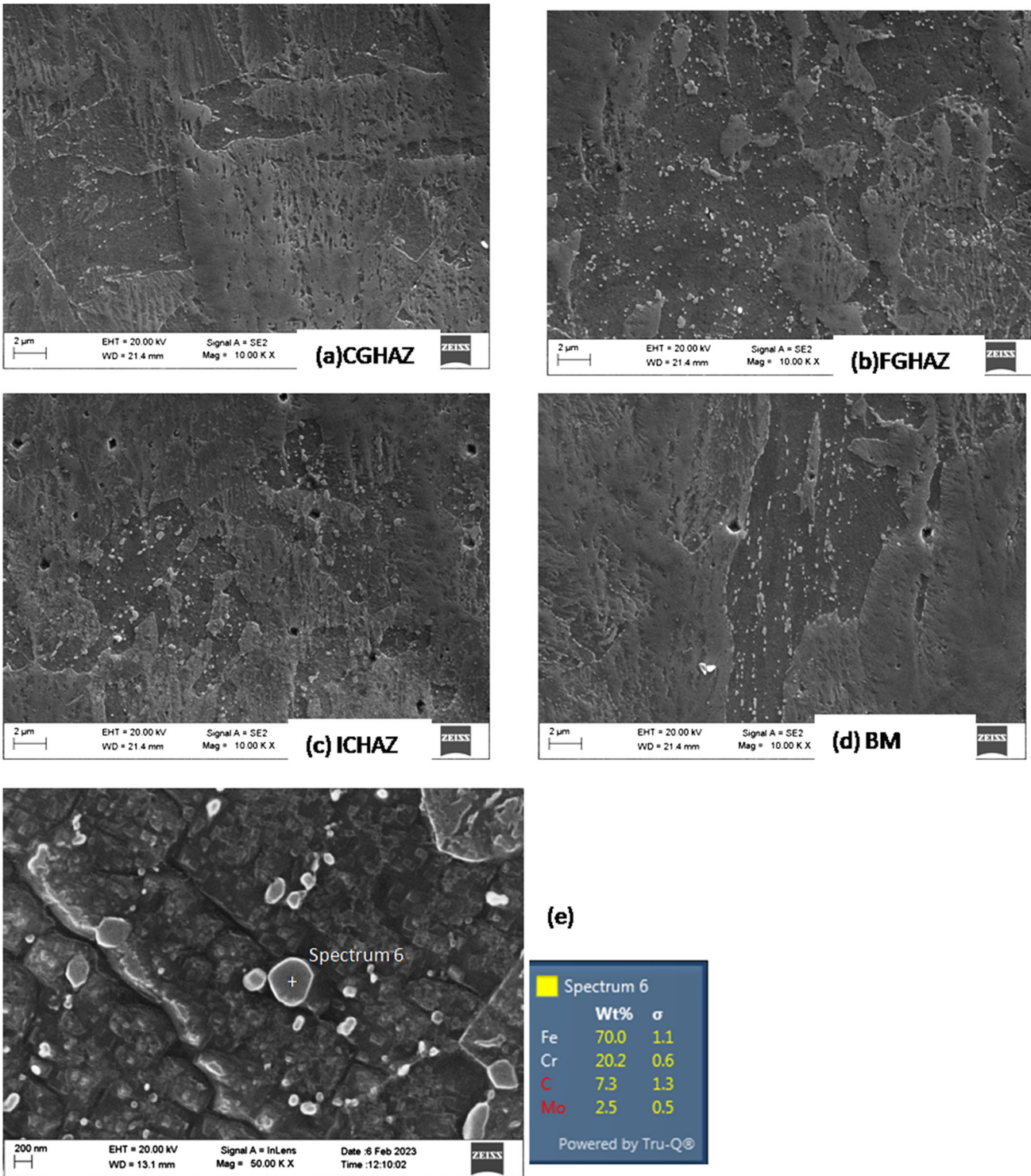


Fig. 5—SEM micrographs of HAZ sub-zones of G91 side after PWHT: (a) CGHAZ, (b) FGHAZ, (c) ICHAZ and (d) G91 base metal (e) high resolution image of carbides at ICHAZ region with EDS result.

B. Hardness Variation Across the Weld Joint

The hardness distributions across the weld joint in the as-weld condition and after PWHT are shown in Figure 6. In the as-weld condition, the fusion zone showed high hardness values due to the possible formation of fresh martensite after welding. Further,

significant hardness variation across the fusion zone was observed due to various phases resulting from rapid cooling. After PWHT, the hardness values in the fusion zone decreased close to base metal values except at very few locations. The decrease in hardness value in the fusion zone after PWHT can be attributed to the general

softening caused by the tempering of the martensite present in the fusion zone.

Furthermore, in the as-weld condition, the hardness values in the G91 steel HAZ region decreased gradually from the region adjacent to the ferritic–weld interface to the outer edge of the HAZ, from ~ 450 to ~ 220 Hv. After PWHT, a considerable reduction in hardness was observed in the HAZ from ~ 230 Hv (adjacent to the weld interface) to ~ 190 Hv (outer edge of the HAZ), which is lower than the unaffected G91 base metal. The base metals showed lower and uniform hardness compared to the fusion zone before and after PWHT. The G91 base metal retains hardness between 210 and 220 Hv without significant reduction following the PWHT. The hardness value of 316LN SS is around 175 to 185 Hv even after PWHT.

C. Microchemical Investigation at the Ferritic Weld Interface

The hardness values near the ferritic–weld interface remained in the range of 350 to 450 Hv even after PWHT (Figure 6). Further, to understand this, EDS spot analysis was carried out on the post-weld heat-treated sample across the G91 steel and weld interface. The results showed a difference in chemical composition in contrast to G91 steel. The interface composition calculated by EDS spot analysis is (11.3Cr–3Ni–0.8Mn–1.1Mo–0.3Si–0.1V–0.1Nb–balance Fe). Since carbon content from EDS analysis is only qualitative, the local carbon content has been evaluated by assuming dilution from both base metals at the interface (25 pct 316 LN SS and 75 pct G91 steel). (The dilution ratio was estimated using the Ni content at the interface contributed by the 316LN SS only since the contribution of Ni from G91 steel is negligible (Ni ≤ 0.22 wt. pct)) Enrichment of Ni and Cr (upto ~ 3 pct) was observed. Being a strong austenite stabiliser, nickel could decrease the A_{c1} transformation temperature of the interface zone. Santella^[19] developed an equation for G91 steel to

predict A_{c1} temperature based on linear regression analysis of the thermodynamic database:

$$A_{c1} (\text{°C}) = 805 + 2.5\text{Cr} + 18.1\text{Mo} + 19.1\text{Si} + 37.1\text{V} + 19.2\text{Nb} - 67.3\text{C} - 130.6\text{N} - 60.5\text{Mn} - 72.3\text{Ni}$$

The A_{c1} temperature of the G91 steel used in the present study based on the above equation is approximately 803 °C (1076 K), and it must be mentioned that the calculated temperature is on par with the A_{c1} temperature reported for G91 steel.^[20] The A_{c1} temperature of the interface based on the input from EDS analysis was found to be as low as 593 °C (866 K). To verify the calculation, the prediction of A_{c1} temperature was also made using JMatPro simulation, as shown in Figure 7. The A_{c1} temperature of G91 steel from simulation showed 805 °C (1078 K), and the G91–weld interface composition showed 500 °C (773 K), thereby decreasing the A_{c1} temperature below the PWHT temperature.

The effect of decrease in A_{c1} temperature on microstructure is studied using EBSD. Figure 8 shows the EBSD-EDS maps of the interface between the fusion zone and G91 steel after PWHT. A phase map is shown in Figure 8(a), where blue and red indicates FCC and BCC phase respectively. It reveals the BCC or FCC phases present but couldn't distinguish between the various BCC phases. Kang *et al.* have shown that Band Slope (BS), a measure of pattern quality in EBSD analysis, exhibits stronger phase contrast than the conventionally used Band Contrast and has qualitatively distinguished the various BCC phases in dual-phase steel.^[21] BS is a quality parameter evaluated by the maximum intensity gradient at the edge of the bands in the pattern. In EBSD patterns, any distortions to the crystal lattice within the diffracting volume produce lower quality (diffused or less sharp) diffraction

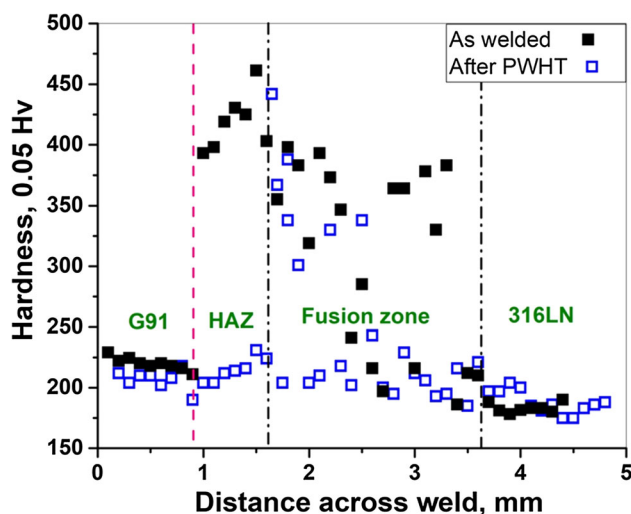


Fig. 6—Hardness variation across the weld joint before and after PWHT.

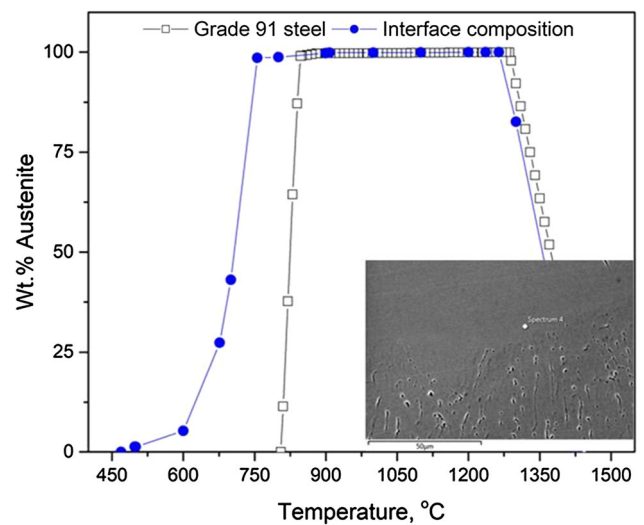


Fig. 7—JMatPro simulation showing the A_{c1} temperature of G91 steel and the G91–weld interface composition (inset showing the location of EDS spot analysis).

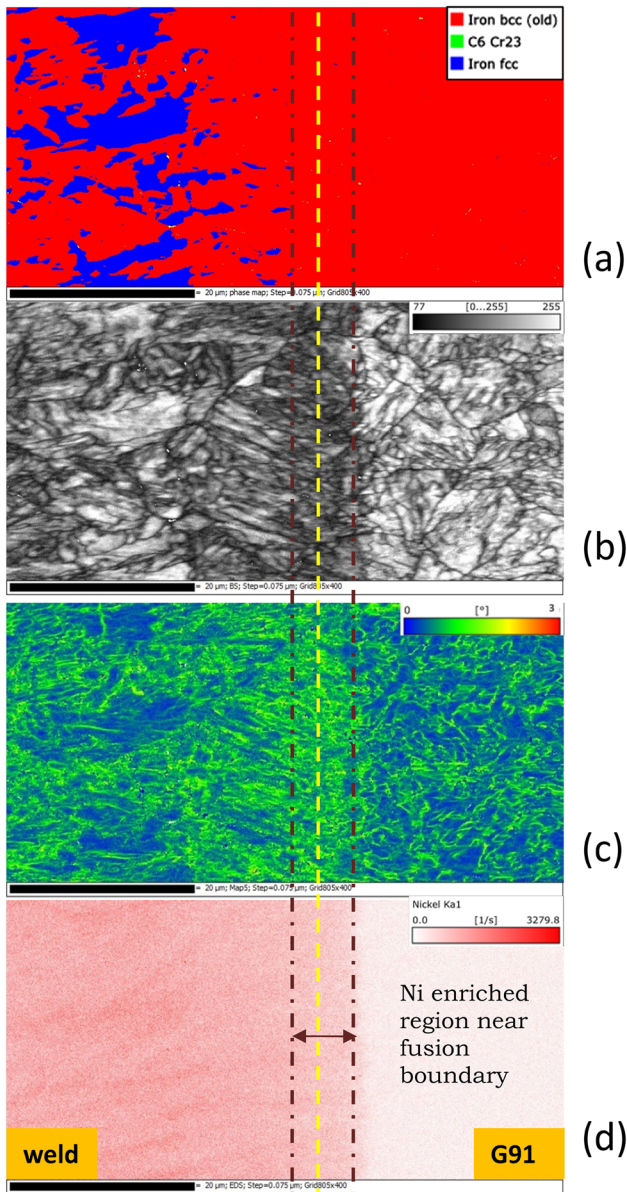


Fig. 8—EBSD results show the presence of fresh martensite in the interface between the weld and G91 steel. (a) Phase map (blue is FCC and red is BCC). (b) Band slope map. (c) Kernel average misorientation map. (d) EDS map showing a variation of nickel content across the fusion boundary.

patterns. This enables the BS map to differentiate the BCC phases qualitatively. The tempered martensite has better image quality, *i.e.* higher BS value than fresh martensite due to the reduced lattice strain upon tempering. Figure 8(b) represents the BS map. A darker region with a lower pattern quality is seen near the interface marked by dotted lines which correspond to fresh martensite formed after PWHT, giving high hardness values (Figure 6). The fresh martensite phase is also distinguished from tempered martensite by its high strain field in the matrix. The presence of fresh martensite can be revealed using Kernel average misorientation (KAM) maps shown in Figure 8(c). The region within the dotted lines has a higher KAM value

(calculated for the 3rd nearest neighbour of each point and upper limit of 5) than the rest of the microstructure. EDS map of nickel distribution alone is shown in Figure 8(d). It shows the dilution of nickel in the fusion zone up to the ferritic–weld interface and its enrichment in the G91 steel. The Ni content in the fusion zone was ~ 7 to 9 wt. pct on average. It is observed up to ~ 3 wt. pct in the G91 steel side close to the fusion boundary. It is to be noted that the Ni content in the G91 steel is negligible (~ 0.22 wt. pct). The dilution of Ni from the 316LN SS side modified the microchemistry of the fusion zone and the ferritic–weld interface, resulting in the evolution of different phases compared to the tempered martensite phase of G91 steel and austenite in 316LN SS as depicted by EBSD phase maps in Figures 8(a) through (c).

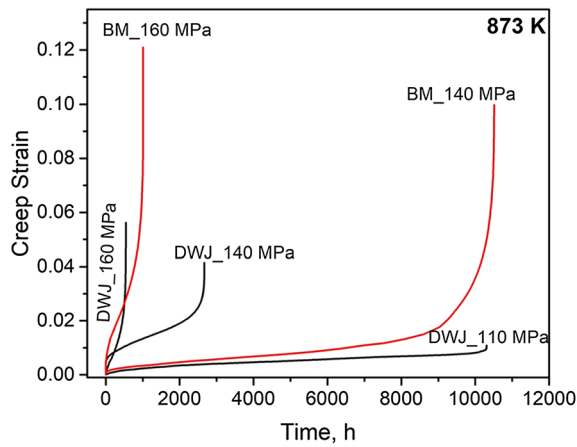
D. Creep Properties of the Weld Joint

The high temperature creep rupture strength of austenitic steels (FCC) is superior to the ferritic–martensitic steels (BCC) due to the low diffusion rate in the austenitic matrix. Among the two base metals, G91 steel has lower creep rupture strength than the 316LN SS, and hence, the creep rupture properties of weld joint are compared with that of G91 steel. The creep curves of the dissimilar weld joint and G91 steel base metal at 873 K are shown in Figure 9(a) and the corresponding creep rupture life plots in Figure 9(b). The weld joint exhibited lower creep rupture strength when compared to the corresponding G91 base metal at all the applied stress levels. Moreover, it may be noted that the slope of the creep rupture strength of weld joint w.r.t rupture life changes with an increase in rupture life, *i.e.*, a decrease in applied stress.

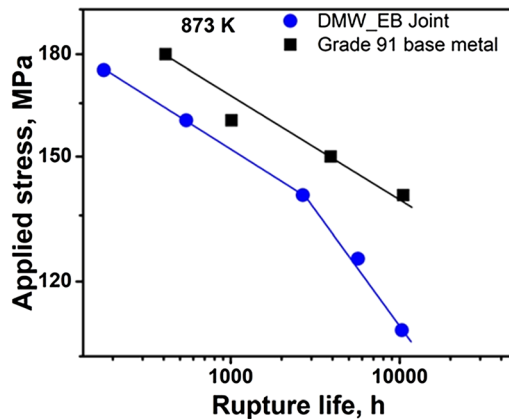
The creep rupture ductility of the weld joint is compared to the ferritic base metal and is shown in Figure 9(c) as a function of rupture life in the form of pct reduction in area. The percentage reduction in area for the base metal is around ~ 80 pct, with a slight decrease in ductility when exposed to longer rupture life, *i.e.*, above 10,000 hours. In the case of the dissimilar weld joint, a sharp decline in pct reduction in area was observed beyond 1000 hours which is consistent with the stress rupture plot. The abrupt decrease in ductility with the change in applied stress implies a changeover in the deformation or fracture failure process discussed subsequently.

E. Failure Location in DWJ and Fractography

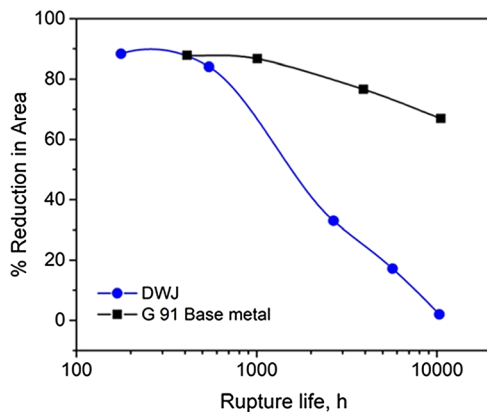
Detailed failure analysis was carried out on creep-tested samples. The creep-ruptured samples of the weld joint are shown in Figure 10. All the joints failed towards the ferritic side of the weld joint. However, the fracture mode and the location of the creep failure varied with the duration of creep exposure. Distinct failure location was observed depending on applied stress level. For the joints tested at high-stress levels of 175 and 160 MPa, the failure location is in G91 steel base metal, and failure is far away from the fusion zone and HAZ region. Excessive necking was seen adjacent to



(a) Creep curves of G91 steel and G91-316LN SS dissimilar weld joint at 873 K



(b) Rupture life comparison of G91 base metal and G91-316LN SS dissimilar weld joint



(c) Comparison of % reduction in area after creep test for G91 base metal and G91-316LN SS dissimilar weld joint

Fig. 9—(a) Creep curves of G91 steel and G91-316LN SS dissimilar weld joint at 873 K. (b) Rupture life comparison of G91 base metal and G91-316LN SS dissimilar weld joint. (c) Comparison of pct reduction in area after creep test for G91 base metal and G91-316LN SS dissimilar weld joint.

the failed region of the sample. The lateral section of the sample tested at 175 MPa is shown in Figure 11(a), which displays substantial necking adjacent to the weld metal without significant reduction in the cross-sectional

area of the fusion zone. Figure 11(b) shows the corresponding scanning electron microscopy (SEM) image of the fractured segment failed by the typical cup and cone fracture, indicating a high pct reduction in area. The fracture surface revealed the typical transgranular fracture characterised by dimples resulting from the coalescence of microvoids (Figure 11(c)).

A distinct fracture appearance was observed at the intermediate stress of 140 MPa. Figures 12(a) and (b) show the fracture surface of the two ends of the sample tested at 140 MPa with shear lips and a flat surface present on the fractured segments. The fractured end where the ferritic ligament was attached to the fusion zone was used to study the longitudinal view of failure, as shown in Figure 12(c). The crack path covered the weld region, HAZ and the ferritic base metal. The shear lip is observed in the ferritic base metal region, indicating the final part of the failure. A series of cavities were observed near the outer edge of the HAZ (marked with an arrow in Figure 12(d)). Similarly, some intermittent sets of cavities (marked with circles) were also observed in the fusion zone close to the ferritic–weld interface. It can be inferred that during testing, the cavities in the HAZ and fusion zone coalesce to form macrocracks which propagated following the above-mentioned preferential path connecting the cavities. The presence of cavities at the outer edge of the HAZ corresponds to the onset of Type IV cracking, which is discussed in the subsequent section. Furthermore, Figure 12(d) clearly demonstrates that the ferritic–weld metal interface is devoid of any coarse carbides, cavities or cracks. Although few cavities were observed in the fusion region in the creep-tested samples, they were limited to a few localised areas. The cavities in the fusion zone were further investigated using SEM as shown in Figure 12(e). EDS spot analysis was performed on regions with bright and dark contrast near cavities. The typical chemical composition as calculated by EDS spot analysis is (12.6Cr–8.0Ni–1.5Mn–1.7Mo–0.3Si–0.1V–0.6S–balance Fe) at bright region and (13.5Cr–4.2Ni–2.1Mo–0.8Mn–0.7Si–0.6S–0.2V–0.1Nb–balance Fe) in dark region.

With the decrease in stress (125 and 110 MPa), *i.e.*, with the increase in the duration of creep exposure, the fracture location shifted to the outer edge of HAZ. A fractography image of the sample tested at 110 MPa revealed a minimal change in cross-sectional area (Figure 13(a)). Figure 13(b) depicts the lateral section of the creep ruptured sample tested at 110 MPa consisting of 316LN SS, fusion zone and ferritic HAZ. The image shows that the weld joint failure tested at 110 MPa occurred 0.55 mm away from ferritic–weld interface at FG/ICHAZ region. Microstructural examination at the vicinity of the failure location (Figure 13(c)) reveals the linking of microcracks. In addition, the microstructure also confirms that in comparison to the $M_{23}C_6$ precipitates seen in PWHT condition (Figures 5(a) through (c)), the $M_{23}C_6$ precipitates within this region had coarsened substantially. The appearance of $M_{23}C_6$ in this location was found to be significantly more spheroidised than those in the other regions of HAZ or base metal. Microstructural



Fig. 10—Creep fracture location of the EB welded dissimilar weld joint specimens tested at 873 K.

observations after creep testing showed that the failure of the joints tested at the stress range of 125 and 110 MPa occurred at the outer edge of the ferritic HAZ. Such low ductility failure occurring in the HAZ is termed a failure by Type IV cracking and is discussed in detail in a review by Abson and Rothwell.^[22]

IV. DISCUSSION

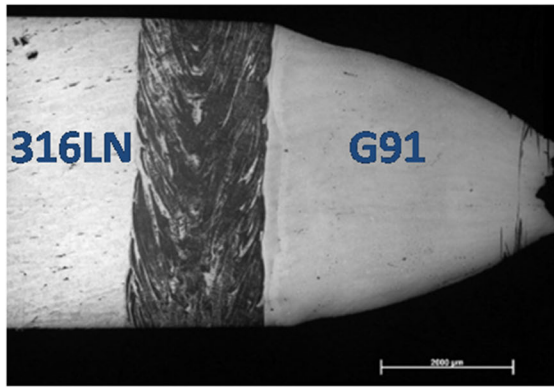
A. Microstructural Evolution Across the Weldment

The detailed microstructural observations in Section III provided insight into the microstructural evolution across dissimilar weldment after welding and PWHT. The optical images (Figure 3) in the as-welded condition across the dissimilar weldment revealed the development of various solidification substructures in the fusion zone which is attributed to the rapid solidification of the molten weld pool and the extent of mixing of the ferritic and austenitic base metals.^[23] Microchemical investigations using EDS spot analysis (Figure 4) showed that the weld is not homogeneous. The inhomogeneous mixing of base metals during welding led to the compositional fluctuations and hence different phases (austenite + martensite + ferrite as predicted by Schaeffler diagram) in the fusion zone.^[23,24] A similar observation in terms of the significant variation in hardness is also noticed across the fusion zone (Figure 6), which is attributed to the multiple phases present. In contrast, the conventional multipass welding processes like SMAW/GTAW where filler wire additions are made, the composition and hardness of the weld metal is homogeneous.^[7-9] In case of GTJs the composition and hardness systematically varies across the weld region.^[25]

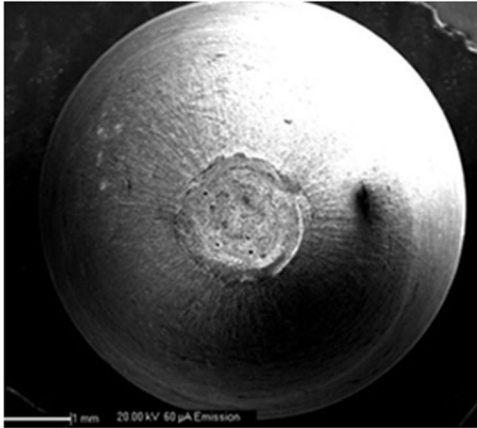
The present study also revealed very high hardness values in the ferritic HAZ region in the as-weld condition, which is attributed to the formation of fresh martensite due to the influence of weld-thermal cycle. The hardness values across the HAZ could be correlated to the peak temperature experienced by the individual location during welding and have been well studied in the literature.^[15,26] In the ferritic HAZ, after PWHT, tempered martensitic structure with a continuous gradient in terms of microstructural features as described in Figures 5(a) through (d) from the fusion zone to

unaffected base metal is observed. After PWHT, the hardness values at HAZ were almost comparable to base metal values except for a minor drop in the ICHAZ. It must be emphasised that the thermal cycle imposed by welding resulting in the FGHAZ/ICHAZ region has a detrimental effect on the optimum distribution of the precipitates and their interparticle spacing, which are initially designed by meticulous alloying and processing and are crucial for the high creep strength of the G91 steel. However, compared to multipass conventional welding methods and in GTJs where HAZ width of 3 to 4 mm is produced,^[15,27-29] electron beam welding produced a narrower HAZ region (0.7 mm) due to its high cooling rate, which is a characteristic of low heat input welding processes.^[29]

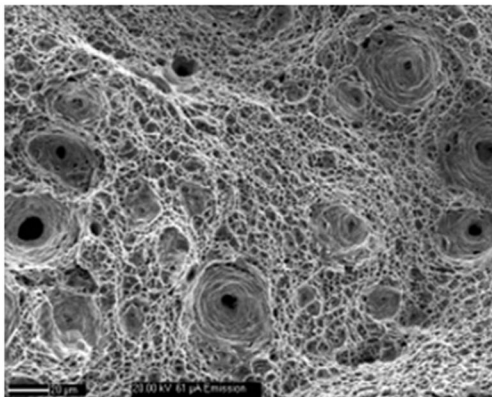
As reported in Figure 6, at certain locations inside the fusion zone and close to ferritic–weld interface, hardness values in the range of 350 to 450 Hv were observed even after PWHT. Similar high hardness values were reported at the interface formed on low alloy ferritic steels using stainless steel and nickel base welding consumables.^[30] Gittos and Gooch have mentioned that the formation of fresh martensite, carbon migration, and coarsened carbides at the interface causes higher hardness.^[30] Similarly, in the present study, the A_{c1} temperature was calculated using Santella's equation^[19] and the prediction of A_{c1} temperature was also made using JMatPro simulation (Figure 7) for the composition at the ferritic–weld interface. The results showed that the A_{c1} temperature is below the PWHT temperature. Consequently, during PWHT at 760 °C (1033 K) for 3 hours, the regions of the weld interface having relatively higher Ni and Cr contents than G91 steel would transform into austenite on heating and subsequently into martensite on cooling. This untempered martensite, which formed freshly at the weld interface, leads to higher hardness in the interface. The EBSD analysis shown in Figure 8 using the band slope map and KAM map confirms the presence of fresh martensite at the narrow region of the ferritic–weld interface. It is, therefore, to be noted that the possibility of a fresh untempered martensitic phase within the fusion zone cannot be excluded since higher hardness is observed in certain regions even after PWHT. In case of novel fabrication methodology like GTJs, the fraction of Ni-rich martensite and thus hardness has been reported to vary systematically from the ferritic–weld boundary



(a) Lateral optical macrograph of the failed DWJ creep specimen tested at 175 MPa.



(b) Fractograph of DWJ creep specimen tested at 175 MPa.



(c) High magnification image of the fractograph showing ductile dimple failure

Fig. 11—(a) Lateral optical macrograph of the failed DWJ creep specimen tested at 175 MPa. (b) Fractograph of DWJ creep specimen tested at 175 MPa. (c) High magnification image of the fractograph showing ductile dimple failure.

for 4 to 5 mm across the functionally graded layers corresponding to the chemical composition of the respective layers.

Based on the results in Sections III-B and III-C, it can be inferred that the ferritic-weld interface possesses a sharp transition in terms of microstructure and hardness compared to the 316LN SS-weld interface.

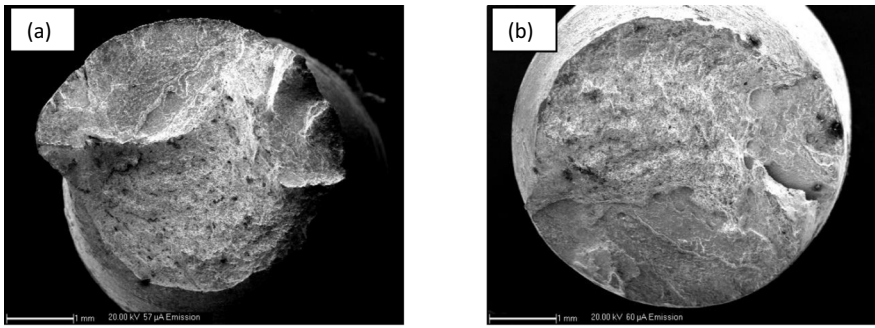
The formation of fresh martensite following PWHT at the ferritic-weld interface in conventional welding techniques is regarded as one of the significant causes of interface failure in such joints during service.^[8,31] Gittos and Gooch have reported that the width of the martensite layer in the conventional welding process (SMAW and SAW) was in the range of 20 to 130 μm when welded with stainless steel base welding consumables and 9 to 15 μm width with nickel base filler wire.^[30] However, in the present case, the fresh martensitic zone is very narrow ($< 10 \mu\text{m}$), assuring better performance under service conditions.

B. Creep Performance of Weld Joint

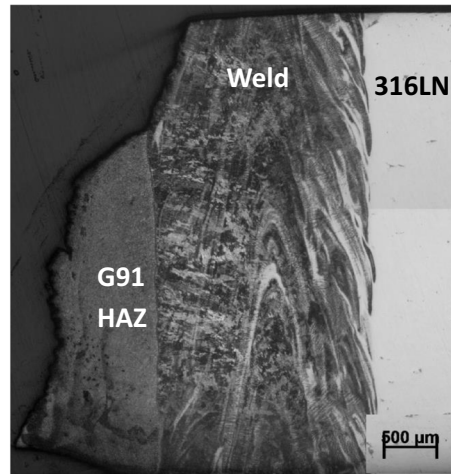
The creep curves of the weld joint and G91 base metal are shown in Figure 9(a). The base metal exhibits the three stages of creep *i.e.* primary, secondary and accelerating tertiary creep regime. The base metal creep failures in ferritic-martensitic steels have been reported due to microstructural degradation caused by coarsening of precipitates and subgrain structures.^[32,33] In the case of weld joints, the gauge length comprises two base metals, HAZs with varying initial microstructure and a fusion zone. Consequently, this leads to inhomogeneous strain accumulation for each region during deformation. On comparing the creep curves at higher stress levels, such as at 160 MPa, it is observed that the creep strain accumulation of the weld joint is lower than the base metal, despite the fact that the weld joint has also failed in the G91 base metal (Figure 9(a)). This is due to the higher creep deformation resistance of 316LN and the fusion zone of the weld joint. With a further decrease in stress to 140 MPa, the creep deformation in weld joints is localised within the HAZ region, as revealed in Figure 10. During deformation, due to the constraints imposed by the adjacent regions in the case of weld joints, the creep deformation behaviour of weld joints is different from that of the base metal. Hence the creep curves vary considerably, and the weld joint shows lower creep strain accumulation than the base metal.

Dissimilar weld joint possessed lower creep rupture life and creep ductility than the G91 base metal (Figures 9(b) and (c)). The stress vs rupture life and ductility plot of weld joint showed sudden decrease in strength and ductility behavior below 140 MPa. In the current investigation, the change in slope of the stress vs rupture plot of the dissimilar weld joint (Figure 9(b)) correlates to the change in failure location of the cross-weld specimen. The joints failed on the ferritic steel side, and the failure site shifted from base metal for stress levels greater than 140 MPa to the ICHAZ region at lower stresses.

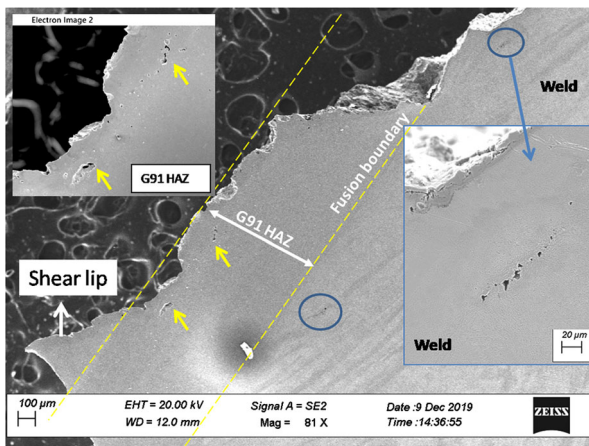
In creep studies, the final location of rupture depends on the weakest region in the gauge length with respect to stress and temperature. At 873 K and high stresses *i.e.* 175 and 160 MPa, the creep failure location is observed at G91 base metal (Figure 11) with a cup and cone type ductile fracture. Similar creep fracture characteristics have been observed in the ferritic steel base metals.^[32,33] However, for specimens with creep exposure of above 2500 hours, *i.e.* stresses below 140 MPa, ICHAZ



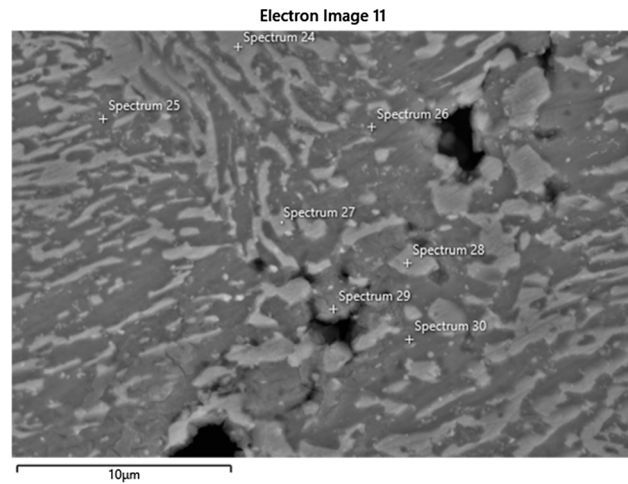
(a, b) Fractographs of creep ruptured DWJ sample tested at 140 MPa.



(c) Lateral optical macrograph of failed DWJ creep specimen tested at 140MPa



(d) SEM Micrograph of failed DWJ creep specimen tested at 140MPa showing cavities in the HAZ (yellow arrow) and inside fusion zone (blue circle).

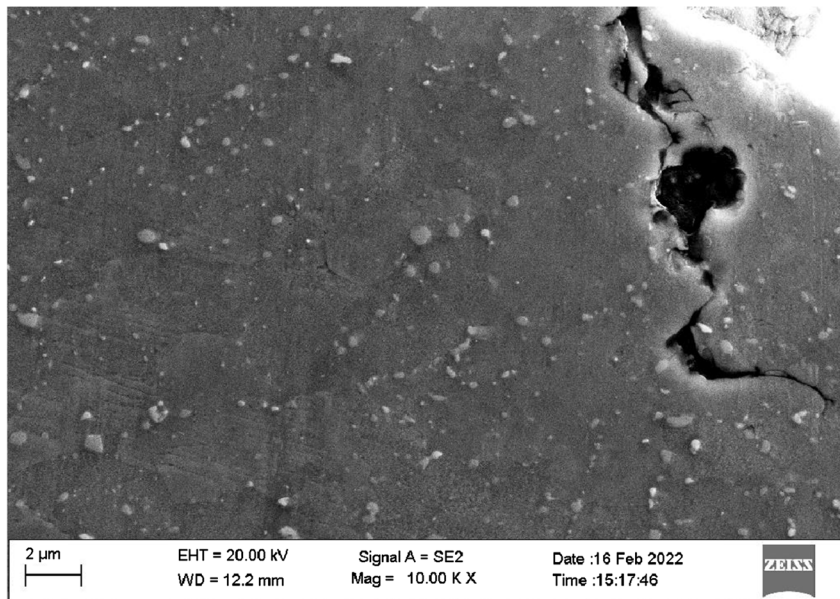
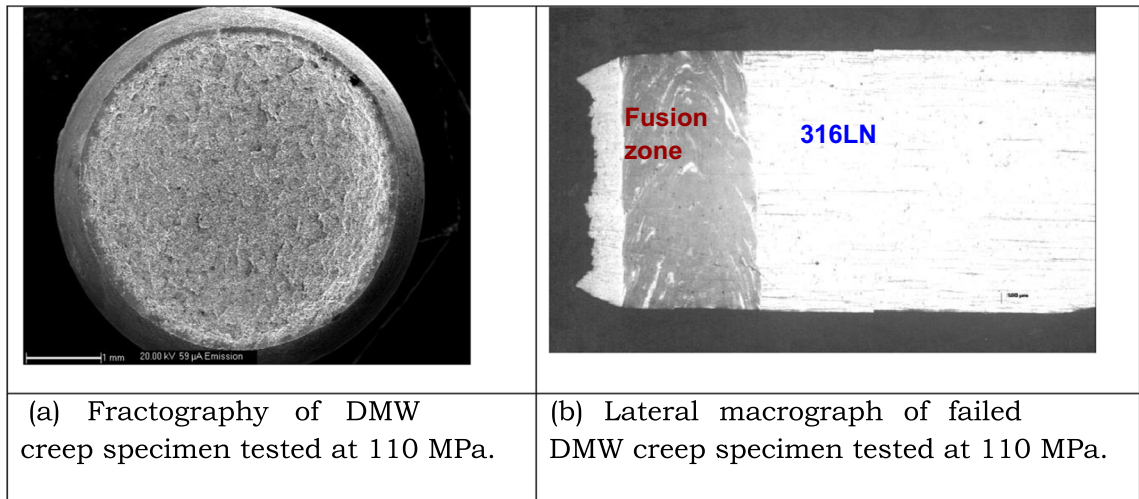


(e) Microstructure showing location of cavities observed in the fusion zone of the creep tested sample.

Fig. 12—(a, b) Fractographs of creep ruptured DWJ sample tested at 140 MPa. (c) Lateral optical macrograph of failed DWJ creep specimen tested at 140 MPa. (d) SEM Micrograph of failed DWJ creep specimen tested at 140 MPa showing cavities in the HAZ (yellow arrow) and inside fusion zone (blue circle). (e) Microstructure showing location of cavities observed in the fusion zone of the creep tested sample.

becomes the weakest region for localized failure and is termed as Type IV failure (Figure 13). Type IV failure has been observed and studied widely in the weld joints

of ferritic–martensitic steels where failure occurs at the fine grain or intercritical region of the HAZ.^[15,26] The cause of Type IV failure has been attributed to the



(c) Micrograph showing micro-cracks and coarsened $M_{23}C_6$ particles adjacent to the failure location of the joint failed at the outer region of the HAZ.

Fig. 13—(a) Fractography of DMW creep specimen tested at 110 MPa. (b) Lateral macrograph of failed DMW creep specimen tested at 110 MPa. (c) Micrograph showing micro-cracks and coarsened $M_{23}C_6$ particles adjacent to the failure location of the joint failed at the outer region of the HAZ.

incomplete transformation in the intercritical region during the weld thermal cycle, which leads to the local softening of the matrix that creates stress triaxiality during creep exposure leading to intense creep cavitation in the intercritical HAZ.

Although the weld chemistry is inhomogeneous in the case of a direct ferritic–austenitic bond, no significant defects or failures were observed in the fusion zone. Few intermittent cavities were observed in the samples tested at 140 to 110 MPa in the fusion zone. A typical micrograph is shown in Figure 12(e). As mentioned earlier in Section III–C, the fusion zone consists of a mixture of phases *i.e.* austenite, tempered martensite

and fresh martensite; it is envisaged that such a zone accommodates the deformation unevenly. The ‘inter-phase’ between the fresh and tempered martensite or between fresh martensite and austenite/ferrite could be the potential nucleation sites for the local damage. However, as the phases formed are not uniformly distributed across the entire volume of the fusion zone, the cavities formed would be difficult to join together to produce cracks or fractures before the onset of Type IV failure.

Regarding the characteristics of creep failure in dissimilar joints of ferritic and austenitic steels, fracture at ferritic–weld interface is of significant concern as it

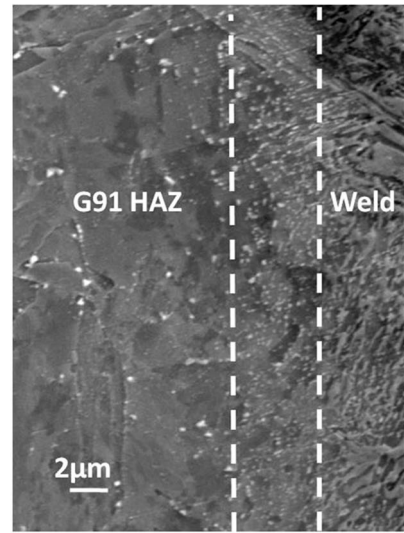
leads to failure of the component prematurely. Few studies have shown that ferritic steel being poor in oxidation resistance, gets preferentially oxidised. Klueh and King have revealed that for low alloy ferritic steel (2¼Cr–1Mo steel) preferential oxidation at the interface is considered one of the significant reasons for interface cracking.^[34] In contrast, high alloy steel with a chromium content of more than 9 wt. pct having quite adequate oxidation resistance, interface cracking due to oxidation may not be considered a prime reason.

Interface cracking, however has also been linked to the carbon migration issues at the ferritic–weld interface. The carbon activity is therefore calculated using ThermoCalc simulations at 873 K for the compositions of ferritic steel (G91), In 82 (Ni-based filler metal) and austenitic stainless steel (316LN SS) and the activity values are 1.7×10^{-4} , 1.8×10^{-4} and 1.7×10^{-5} respectively. The carbon activity of ferritic and austenitic stainless steel differ by an order of magnitude whereas Ni-based filler wire has carbon activity value close to that of ferritic steel. Thus, the use of Ni-based welding consumables are being sought to reduce the carbon migration issue with the ferritic steels.^[4–6]

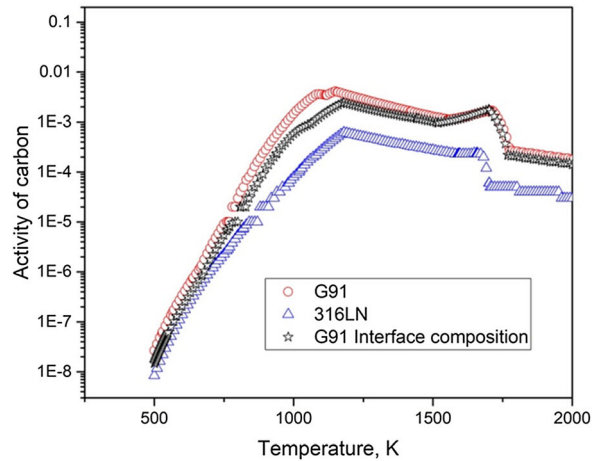
DuPont reviewed the microstructural evolution at the ferritic–austenitic dissimilar joint interface and discussed how the formation of coarse carbides at the interface leads to the evolution of cavity nucleation around it, citing this as one of the critical causes of interface failure even with Ni-based welding consumables.^[10] Researchers have reported such interface failures above 3000 hours of creep exposure at 823 K.^[8,9] In the current investigation, at 873 K for the specimen that ruptured at 10,295 hours, fine and randomly dispersed carbides could be observed at the interface (Figure 14(a)) rather than a string of coarse carbides as described in the literature for conventional multipass weld joints. As EB welding technique is a low heat input process compared to the conventional multipass welding techniques, the interface stability is improved. To address the interface stability of this dissimilar joint, carbon activity in the base metals (G91 and 316 LN SS) and the composition close to the ferritic interface were computed using ThermoCalc and plotted as a function of temperature, as shown in Figure 14(b). Although the figure shows some difference in carbon activity between 316LN SS and G91 steel, the composition at the ferritic–weld interface exhibits almost equivalent carbon activity to G91 steel. This improved the interface’s stability by impeding the diffusion kinetics leading to coarsening of the carbides like $M_{23}C_6$, M_6C , etc., reported at the interface of DWJs fabricated by conventional welding techniques.

C. Weld Strength Reduction Factor (WSRF)

Weld joints are the life-limiting stress concentration sites in mechanical structures, and they reduce the long-term creep rupture strength significantly. The creep design of welded components addresses this issue by incorporating a weld strength reduction factor (WSRF)



(a) Microstructure showing absence of cavitation at the interface of G91/Weld metal after creep test at 110 MPa.



(b) Carbon activity profile with respect to temperature for base metals and ferritic–weld interface composition.

Fig. 14—(a) Microstructure showing absence of cavitation at the interface of G91/Weld metal after creep test at 110 MPa. (b) Carbon activity profile with respect to temperature for base metals and ferritic–weld interface composition.

to compute the allowable design stress for the welded components. WSRF is defined as the ratio of the uniaxial creep rupture strength of the weld joint to the base metal’s creep rupture strength at the same rupture life, temperature and environment. The variation of WSRF with creep rupture life of EB welded dissimilar joint between G91 steel and 316LN SS at 873 K from this study was calculated and presented in Figure 15. It shows the loss of creep rupture strength of the DWJ with the increase in creep exposure time. A marginal loss of 5 to 10 pct of creep rupture strength of the joint (WSRF above 0.9) compared to the base metal was observed at the initial stage of about 1000 hours of creep exposure. But once Type IV failure starts, WSRF is close to 0.8 at 10^4 hours. This result is compared with the data in the literature^[35] for a dissimilar joint

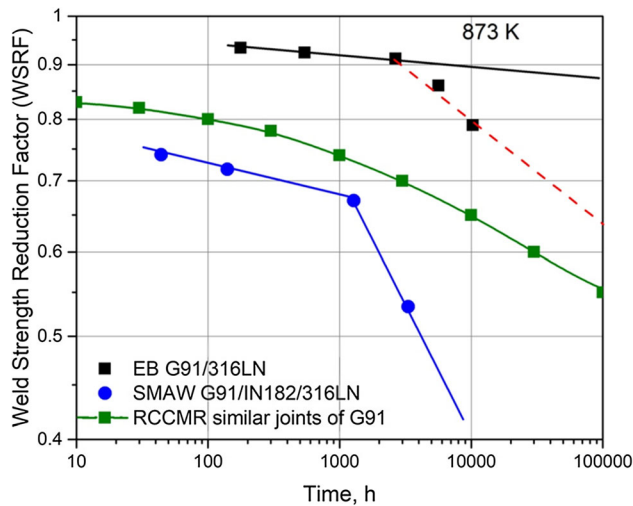


Fig. 15—The variation of weld strength reduction factor (WSRF) with time at 873 K for EB welded DWJ and its comparison with the DWJ fabricated by SMAW technique.

fabricated by the technique recommended in the standards, *i.e.* by SMAW using IN182 electrode between G91 and 316LN SS at 873 K. The WSRF values were observed to be below 0.7 and reached to 0.533 at 3300 hours of creep exposure. In ASME, the stress rupture factor of a similar joint of G91 steel welded using either SFA-5.28 ER90S-B9, SFA-5.5 E90XX-B9, or SFA-5.23 EB9 electrodes is 0.84 at 873 K.^[36] In RCC-MRx,^[37] the stress rupture factor specified as “coefficient Jr” is given as a function of time, for a similar joint of G91 steel, prepared by TIG process using a mod. 9Cr filler wire is shown in Figure 15. It must be mentioned that the RCC-MRx curves are generated from a large database, and the WSRF values are obtained following statistical treatment of the data, and finally, the lower bound values are adopted by the standard. In comparison to RCC-MRx data of a similar joint at 10^4 hour, the EB welding technique exhibited a 21 pct increase in weld strength reduction factor. The current study, however, presents a single set of data which is generated systematically at 873 K by controlling creep test temperature within ± 2 K and by calibration of machines prior to each test. It is important to establish large creep database over a wide range of stresses and temperatures to apply WSRF data for the design of EB welded components.

The creep rupture life of the dissimilar welded joint was approximately 10 times longer than the DWJ prepared by the conventional welding technique (SMAW) at 873 K.^[35] The results thus reveals that EB welded dissimilar joints between 316LN SS and G91 steel possess improved creep properties with high weld strength reduction factor. Therefore, the current investigation results emphasise that the improvement in creep rupture characteristics of the DWJ can be achieved by a high energy density—low heat input process in a single pass, such as EB welding technique.

V. SUMMARY

The manuscript presents microstructural investigations on dissimilar joint (DWJ) between G91 and 316LN SS, prepared by autogenous EB welding technique, and the creep rupture characteristics of the DWJ at 873 K. The important observations are summarised below:

1. The fusion zone revealed compositional variations with distinct microstructural features depending on the extent of mixing of ferritic and austenitic base metals.
2. At the ferritic–weld interface, Ni enrichment up to ~ 3.0 wt. pct is observed, leading to the formation of fresh untempered martensite of $< 10 \mu\text{m}$ width upon PWHT.
3. The weld joint exhibited lower creep rupture strength when compared to the corresponding G91 base metal at all the applied stress levels.
4. The DWJs failed on the ferritic steel side, and the failure location changed from base metal (for stresses ≥ 160 MPa) to the outer edge of the HAZ region where type-IV crack is observed for longer creep exposures.
5. Interface failures were not observed in the present study owing to insignificant cavitation or coarsening of carbides at the ferritic–weld interface.
6. The DWJ fabricated by Electron beam welding exhibited good creep resistance at 873 K and showed high weld strength reduction factor that varied from 0.9 to 0.8 with increasing creep exposure up to 10,000 hours.

CONFLICT OF INTEREST

On behalf of all authors, the corresponding author states that there is no conflict of interest.

REFERENCES

1. R.W. Evans and B. Wilshire: *Mech. Mater.*, 1985, vol. 4, pp. 51–65.
2. C.D. Lundin: *Weld. J.*, 1982, vol. 6, pp. 58–63.
3. A.K. Bhaduri, S. Venkadesan, P. Rodriguez, and P.G. Mukunda: *Int. J. Press. Vessel. Pip.*, 1994, vol. 58, pp. 251–65.
4. J. Kucera, J. Vrestál, and K. Stránský: *Defect. Diffus. Forum*, 1991, vol. 66–69, pp. 1395–400.
5. R. Anand, C. Sudha, S. Saroja, and M. Vijayalakshmi: *Metall. Mater. Trans. A Phys. Metall. Mater. Sci.*, 2013, vol. 44, pp. 2156–70.
6. F. Gauzzi and S. Missori: *J. Mater. Sci.*, 1988, vol. 23, pp. 782–89.
7. J.D. Parker and G.C. Stratford: *Mater. Sci. Eng. A*, 2001, vol. 299, pp. 164–73.
8. K. Laha, K.S. Chandravathi, P. Parameswaran, S. Goyal, and M.D. Mathew: *Metall. Mater. Trans. Phys. A Metall. Mater. Sci.*, 2012, vol. 43, pp. 1174–86.
9. T. Sakthivel, P. SyamalaRao, P.K. Parida, and M. Vasudevan: *Mater. Lett.*, 2022, vol. 306, pp. 1–4.

10. J.N. DuPont: *Int. Mater. Rev.*, 2012, vol. 57, pp. 208–34.
11. J. Vekeman, S. Huysmans, and E. De Bruycker: *Weld. World*, 2014, vol. 58, pp. 873–82.
12. M. Subramanian, J. Galler, J. DuPont, B. Kombaiah, X. Yu, Z. Feng, and S.S. Babu: *Weld. World*, 2021, vol. 65, pp. 1633–44.
13. H. Wang and E. Lara-curzio: *Pressurized Tube Creep Testing of Graded Transition Joints (GTJ) for G91 and 347H Base Metals*, No. ORNL/TM-2022/2568, Oak Ridge National Lab.(ORNL), Oak Ridge, TN, 2022.
14. A. Kulkarni, D.K. Dwivedi, and M. Vasudevan: *Weld. J.*, 2021, vol. 100, pp. 269–s–80-s.
15. K. Laha, K.S. Chandravathi, P. Parameswaran, K.B.S. Rao, and S.L. Mannan: *Metall. Mater. Trans. A Phys. Metall. Mater. Sci.*, 2007, vol. 38, pp. 58–68.
16. R.E. Avery: *Pay Attention to Dissimilar-Metal Welds: Guidelines for Welding Dissimilar Metals*, Nickel Development Institute, 1991.
17. Z. Sun and R. Karppi: *J. Mater. Process. Technol.*, 1996, vol. 59, pp. 257–67.
18. A.L. Schaeffler: *Met. Progress*, 1949, vol. 56, p. 680.
19. M.L. Santella: *J. Press. Vessel Technol. Trans. ASME*, 2012, vol. 134, pp. 1–5.
20. B. Jeya Ganesh, S. Raju, A.K. Rai, E. Mohandas, M. Vijayalakshmi, K.B.S. Rao, and B. Raj: *Mater. Sci. Technol.*, 2011, vol. 27, pp. 500–12.
21. J.Y. Kang, S.J. Park, and M.B. Moon: *Microsc. Microanal.*, 2013, vol. 19, pp. 13–16.
22. D.J. Abson and J.S. Rothwell: *Int. Mater. Rev.*, 2013, vol. 58, pp. 437–73.
23. S. Kou: *Weld Metallurgy*, Wiley, 1972, pp. 255–57.
24. P.S. Liu, W.A. Baeslack III., and J. Hurley: *Weld. J.*, 1994, vol. 73, pp. 175–81.
25. J.P. Galler, J.N. DuPont, S.S. Babu, and M. Subramanian: *Metall. Mater. Trans. A Phys. Metall. Mater. Sci.*, 2019, vol. 50, pp. 2201–17.
26. J. Parker: *Mater. Sci. Eng. A*, 2013, vol. 578, pp. 430–37.
27. Y. Wang, R. Kannan, and L. Li: *Mater. Des.*, 2020, vol. 190, 108570.
28. H.C. Dey, S.K. Albert, A.K. Bhaduri, G.G. Roy, R. Balakrishnan, and S. Panneerselvi: *Weld. World*, 2014, vol. 58, pp. 389–95.
29. M. Divya, C.R. Das, S.K. Albert, S. Goyal, P. Ganesh, R. Kaul, J. Swaminathan, B.S. Murty, L.M. Kukreja, and A.K. Bhaduri: *Mater. Sci. Eng. A*, 2014, vol. 613, pp. 148–58.
30. M. Gittos and T. Gooch: *Weld. J.*, 1992, vol. 71, p. 461.
31. J.N. DuPont and C.S. Kusko: *Weld. J.*, 2007, vol. 86, pp. 51–54.
32. T. Shrestha, M. Basirat, I. Charit, G.P. Potirniche, and K.K. Rink: *Mater. Sci. Eng. A*, 2013, vol. 565, pp. 382–91.
33. J. Vanaja, K. Laha, R. Mythili, K.S. Chandravathi, S. Saroja, and M.D. Mathew: *Mater. Sci. Eng. A*, 2012, vol. 533, pp. 17–25.
34. R.L. Klueh and J.F. King: *Weld. J. (Miami FL)*, 1982, vol. 61, pp. 302–11.
35. D.D. Awale, A.R. Ballal, M.M. Thawre, V.D. Vijayanand, and G.V. Reddy: *Trans. Indian Natl Acad. Eng.*, 2022, vol. 7, pp. 449–456.
36. ASME, Section III, Division I-NH: *Boiler and Pressure Vessel Code*, The American Society of Mechanical Engineers, New York, 2013.
37. RCC-MRx: *Design and Construction Rules for Mechanical Components of Nuclear Installations*, Section III, subsection. Z. AFCEN, Paris, 2012.

Publisher's Note Springer Nature remains neutral with regard to jurisdictional claims in published maps and institutional affiliations.

Springer Nature or its licensor (e.g. a society or other partner) holds exclusive rights to this article under a publishing agreement with the author(s) or other rightsholder(s); author self-archiving of the accepted manuscript version of this article is solely governed by the terms of such publishing agreement and applicable law.